MNRAS **000**, 1–?? (2020) Preprint 28 September 2020 Compiled using MNRAS LATEX style file v3.0

Equation of State of Hot Dense Hyperonic Matter in the Quark-Meson-Coupling (QMC-A) model

J. R. Stone, [1,2] V. Dexheimer,[3] P. A. M. Guichon,[4] and A. W. Thomas,[5]
[1] *Department of Physics and Astronomy, University of Tennessee, Knoxville, TN 37996, USA*
[2] *Department of Physics (Astrophysics), University of Oxford, Keble Road OX1 3RH, Oxford, UK*
[3] *Department of Physics, Kent State University, Kent, OH 44243 USA*
[4] *DPhN, IRFU-CEA, Université Paris-Saclay, F91191 Gif sur Yvette, France*
[5] *CSSM and CoEPP, School of Physical Sciences, University of Adelaide, Adelaide SA 5005, Australia*

Accepted XXX. Received YYY; in original form ZZZ

ABSTRACT

We report a new equation of state (EoS) of cold and hot hyperonic matter constructed in the framework of the quark-meson-coupling (QMC-A) model. The QMC-A EoS yields results compatible with available nuclear physics constraints and astrophysical observations. It covers the range of temperatures from T=0 to 100 MeV, entropies per particle S/A between 0 and 6, lepton fractions from Y_L=0.0 to 0.6, and baryon number densities n_B=0.05-1.2 fm^{-3}. Applications of the QMC-A EoS are made to cold neutron stars (NS) and to hot proto-neutron stars (PNS) in two scenarios, (i) lepton rich matter with trapped neutrinos and (ii) deleptonized chemically equilibrated matter. We find that the QMC-A model predicts hyperons in amounts growing with increasing temperature and density, thus suggesting not only their presence in PNS but also, most likely, in NS merger remnants. The nucleon-hyperon phase transition is studied through the adiabatic index and the speed of sound c_s. It is shown that the lowering of $(c_s/c)^2$ to and below the conformal limit of 1/3 is a general consequence of instabilities due to any phase transition and is not a unique fingerprint of the hadron-quark matter transition. Rigid rotation of cold and hot stars, their moments of inertia and Kepler frequencies are also explored.

The QMC-A model results are compared with two relativistic models, the chiral mean field model (CMF), and the generalized relativistic density functional with hyperons (GRDF-Y). Similarities and differences are discussed.

Key words: stars: neutron – equation of state – dense matter – stars: evolution

1 INTRODUCTION

Properties of young proto-neutron stars (PNS) born in core-collapse supernovae (CCSN) have been one of the main topics of interest in observation and theoretical modeling for a long time (Burrows & Lattimer (1986); Prakash et al. (1997); Pons et al. (1999)). Recently, the topic has resurfaced in the context of the possible emission of detectable gravitational waves (GW) in CCSN events (Ferrari et al. (2003); Camelio et al. (2017); Torres-Forné et al. (2019)). Better understanding of both static and dynamic properties of neutron stars (NS) will support an increasing interest in the emission of continuous GW from neutron star candidates in young supernova remnants Lindblom & Owen (2020). More generally, hot dense matter and its composition is particularly relevant in the context of binary neutron star mergers (BNSM) (Abbott et al. (2017); Baiotti & Rezzolla (2017); Abbott et al. (2018); Most et al. (2020); Bauswein et al. (2019)).

There has been an extensive discussion concerning the appearance of non-nucleonic species in high density matter, such as strange baryons (hyperons), pion and kaon condensates, and various phases of quark matter, together with their density and temperature dependence (Balberg et al. (1999); Pons et al. (1999, 2001); Mishra et al. (2010); Chatterjee & Vidaña (2016); Oertel et al. (2016, 2017); Roark et al. (2019); Malfatti et al. (2019)). The effects of finite temperature were first studied by Goussard et al. (1998). They restricted the solutions to several cases of chemically equilibrated nucleonic matter at fixed temperature and/or entropies with overall fixed lepton fractions. More recently, the finite temperature high density matter in CCSN and PNS, including nucleons, Λ, $\Sigma^{0,+,-}$ and $\Xi^{0,-}$ hyperons (the full baryon octet) and free thermal pions, was studied in by Ishizuka et al. (2008) in the framework of an extended $SU_f(3)$ relativistic mean model (RMF). Three new EoS la-

beled EOSY were constructed and tables computed in a wide range of charge ratios, baryon densities and temperatures, mainly designed for CCSN models.

The new EoS tables were later adopted by Sumiyoshi et al. (2009) in their simulation of the dynamical collapse of a non-rotating massive stars. The exploration of the time dependence of the hyperon appearance in stages of the initial collapse, core bounce, and a temporary proto-neutron evolution before collapsing to a black hole revealed a significant hyperon content (mostly Λ and Ξ^-) in the center of the star 680 ms after bounce, after being mostly located at about 10 km off center at 500 ms.

A somewhat simplified variant of the QMC model (different from that used in the present work) has been used by Panda et al. (2010) to explore neutrino-free matter and matter with trapped neutrinos in PNS at fixed temperatures up to 20 MeV and fixed entropy per particle S/A = 1 and 2. In comparison with the non-linear Walecka model with GM1 parameterization, QMC predicted smaller strangeness and neutrino fractions, however, growing faster with increasing temperature and density.

Shen et al. (2011) constructed three EoS tables for CCSN simulations, assuming matter composed of nucleons and Λ hyperons, in the framework of the RMF theory. They found that the population of Λ hyperons increases with temperature and is distributed over the whole stellar-core density range at T=100 MeV, where it constitutes 16% for the proton fraction Y_p=0.1. Burgio et al. (2011) constructed an EoS for hyperonic matter at finite temperature using the Bruckner-Hartree-Fock (BHF) method with V18+UIX nucleon-nucleon and the NSC89 nucleon-hyperon interactions. Only Λ and Σ^- hyperons were predicted up to high densities when S/A was chosen to be 1 and 2. It was shown that the density threshold found for the appearance of hyperons at zero temperature do not exist at finite temperature and hyperons are present at all densities in the star core. The hyperonic content in matter with trapped neutrinos was found to be lower than in the neutrino free chemically-equilibrated matter.

Numerical simulations of BNSM both with nucleonic and hyperonic EoS with Λ hyperons were performed by Sekiguchi et al. (2011), who predicted a substantial role of hyperons in post-merger dynamics and suggested a possibility that the presence of hyperons may be imprinted in the evolution of the characteristic frequency of GW and the peak width of the GW signal. Oertel et al. (2012) modified the widely used Lattimer-Swesty EOS (Lattimer & Douglas Swesty (1991)) by including hyperons, pions and muons to the high density part of the EoS and showed that the additional degrees of freedom influence the thermodynamic properties such as pressure, energy density, and the speed of sound in a non-negligible way. The EoS including Λ hyperons in dense matter, based on GRDF-Y with the DD2Y interaction (Typel et al. (2010)), developed by Banik & Char (2014), and the EoS including the whole baryon octet and decuplet and allowing for chiral symmetry to be restored, constructed by Dexheimer & Schramm (2008), predicted the maximum gravitational mass of a cold neutron star to be > 1.9 $M_\odot$, consistent with observations at the time. These results were in contrast will previously published EoS with hyperons (Ishizuka et al. (2008); Sumiyoshi et al. (2009); Shen et al. (2011); Burgio et al. (2011); Oertel et al. (2012)), which predicted the maximum mass of the cold NS below that limit. These EoS predicted a large population of hyperons in dense uniform matter, at the cost of neutrons, growing with increasing temperature. The latest model of dense matter at finite temperatures was constructed by Marques et al. (2017) in the RMF framework. The authors also examined hypermassive NSs in the post-merger phase of BNSM and the moment of inertia-quadrupole moment (I-Q) universality. They found this universality was broken in fast rotating stars when thermal effects became important.

Despite the great variety of models and approaches in the literature, a general consensus on the EoS and composition of either cold or hot high density matter in the core of (proto)neutron stars, *based on microphysics*, has not been achieved as yet (Stone et al. (2016)). The reason is that the nuclear and particle physics input to modeling of the EoS is poorly understood and there are no terrestrial data directly applicable to the high-density low-temperature sector of the QCD diagram (Sharma (2019)). The most recent trend in the field of study of EoS points toward statistical methods, such as Bayesian analysis (Nättilä et al. (2016); Raaijmakers et al. (2018); Lim & Holt (2019); Greif et al. (2019)), parametric representations based on observational data (e.g. Özel & Freire (2016); Lindblom (2018); Mena-Fernández & González-Romero (2019)), or machine learning methods (e.g. Fujimoto et al. (2018); Weih et al. (2019); Fujimoto et al. (2020)). However, this trend leaves many questions related to the underlying quark structure of hadrons in dense matter unanswered.

In this work we report a new microscopic EoS of hot high-density hyperonic matter using the latest QMC-A model based on the model detailed in (Guichon et al. (2018)) extended to finite temperature. The model is fundamentally different from other mean-field microscopic models used up to now, as outlined in Sec. 2, and provides a natural explanation to some open questions in low energy nuclear structure physics. The QMC-A model predictions of properties of static cold NS are presented in Secs. 3.1.1 and 3.2.1 and for hot PNS in Sec. 3.1.2 and 3.2.2, compared with the outcome of the chiral mean field model (CMF) (Dexheimer & Schramm (2008); Roark et al. (2019)), and the extended GRDF-Y model with the DD2Y interaction (Typel et al. (2010); Typel (2020)). The nucleon-hyperon phase transition and its consequence for the stability of the star, together with the speed of sound, in both cold and hot stars are shown in these sections. Effects of uniform rotation on the stars' mass, radius and composition, as well as the universal relations between the moment of inertia and the star mass and compactness, are illustrated in Sec. 4. Discussion of the results and outlook can be found in Sec. 5.

2 THE METHOD

2.1 The QMC-A model

In the QMC framework (Guichon (1988); Guichon et al. (1996)), the effect of the dense medium surrounding nucleons and hyperons in the dense stellar core on their interaction is modeled by dynamics of the quarks inside individual particles. In other words, the quarks in a nucleon (or hyperon) interact *self-consistently* with the quarks in surrounding particles via exchange of σ, ω, and ρ virtual mesons. This is

fundamentally different from the RMF-like models, where the exchange of mesons proceeds between point-like particles with no internal structure. The first version of the relativistic QMC model applied to NS (Rikovska-Stone et al. (2007)) predicted the existence of cold NS with Λ and Ξ^0 hyperons in their cores with a maximum mass of 1.97 $M_\odot$, three years before such a star was observed by Demorest et al. (2010) (later updated by Fonseca et al. (2016)). The non-relativistic application of the QMC model to finite nuclei yielded predictions of ground state properties of finite nuclei (Stone (2016); Martinez et al. (2019); Stone et al. (2019); Martinez et al. (2020)) in excellent agreement with experimental data.

The QMC-A model has a unique set of four variable parameters, the meson-nucleon couplins to the non-strange quarks, which are conveniently expressed as the coupling constants in free space $G_{\sigma N}$, $G_{\omega N}$, $G_{\rho N}$ and the mass of the σ meson M_σ. These parameters generated data, consistent with saturation properties of symmetric nuclear matter and observational data on NS, including the maximum mass and radius/tidal deformation of a 1.4 $M_\odot$ star. The coupling constants used in the present work are $G_{\sigma N}$=10.33 fm^2, $G_{\omega N}$= 6.095 fm^2, $G_{\rho N}$= 2.91fm^2, and M_σ=700 MeV. Because in our case the forces acting in dense matter are between quarks and not between the particles as entities, there is no need to increase the number of parameters when the baryonic composition changes. Thus, matter consisting of only nucleons or of the entire baryon octet is modeled by the same parameter set. Once determined, the set is fixed and cannot be varied to improve the predictive power of the model. Should a discrepancy between the model prediction and new observational and experimental data occur, missing physics in the model must be sought.

The latest version of the model, called QMC-A, is an extension of the original model for T=0, described in detail in Ref. (Guichon et al. (2018)). The formalism has been extended to finite temperatures with and without neutrinos and includes a smooth transition between T=0 and T>0 cases. The present work includes a new treatment of the sigma field and a complete self-consistent treatment of Fock terms, which will be described elsewhere. QMC-A EoS complies with the commonly accepted constraints on the isospin-symmetric nuclear matter at saturation (Tsang et al. (2012); Horowitz et al. (2014); Stone et al. (2014)) yielding a saturation density n_0=0.156 fm^{-3}, saturation energy E/A=-16.2 MeV, symmetry energy J=28.5 MeV, slope of the symmetry energy L=54 MeV, and incompressibility K=292 MeV.

2.2 Calculation details

All calculations in this work have been performed assuming a full chemical and thermal equilibrium, and the charge neutrality being strictly conserved. For a system consisting of the octet baryons and leptons $(e^-, \bar{\nu}_e, e^+, \nu_e), (\mu^-, \bar{\nu}_\mu, \mu^+, \nu_\mu)$, we calculate chemical potentials of all the constituents, consequently used to derive other thermodynamical quantities. Further assuming lepton number conservation, the system is described by the lepton fraction $Y_L = (L_e + L_\mu)/n_B$ where electron, L_e, and muon, L_μ, lepton number densities are supposed to be known and enter the equilibrium and charge conservation relations

$$\mu(e^-) - \mu(\nu_e) = \mu(\mu^-) - \mu(\nu_\nu)\,, \quad (1)$$

$$\mu(i) = \mu(n) - Q(i)\mu(e^-) + Q(i)\mu(\nu_e)\,, \quad (2)$$

and

$$n(e^-) + n(\nu_e) - n(e^+) - n(\bar{\nu}_e) = L_e\,, \quad (3)$$

$$n(\mu^-) + n(\nu_\mu) - n(\mu^+) - n(\bar{\nu}_\mu) = L_\mu\,, \quad (4)$$

$$n(e^+) - n(e^-) + n(\mu^+) - n(\mu^-) = -\sum_i n(i)Q(i)\,, \quad (5)$$

$$\sum_i n(i) = n_B\,, \quad (6)$$

where $n(i)$, $\mu(i)$ and $Q(i)$ are particle number densities, chemical potentials and charges of a baryon constituent i, respectively. This scenario corresponds to dense matter with trapped neutrinos, believed to exist, at least to a certain extend, just after the bounce in the CCSN event. The system can be modeled at fixed values of Y_L and temperature/entropy per particle. Although in the dynamic development of a PNS during this regime, a thermodynamic equilibrium is not likely to be fully observed, this is the approximation we take. As we do not have neutrino transport built in the model to inform us about the changing number of neutrinos in the system, there is no other self-consistent way to determine Y_L.

When the PNS is older than a few minutes, the temperature of the star is low enough that the neutrinos can leave freely, neutrino chemical potential becomes zero, and the lepton number is no longer conserved. Matter goes through a process called deleptonization (Burrows et al. (1981)). The loss of neutrinos is accompanied by a loss of electrons through electron capture. The chemical equilibrium shifts matter to become more neutron rich and the number of free leptons decreases considerably. The diffusion of neutrinos from the core, which lasts a few seconds results in a significant heating of the core (Burrows & Lattimer (1986)). Deleptonized matter mater in the chemical equilibrium is governed by equations

$$\mu(e^-) = \mu(\mu^-)\,, \quad (7)$$

$$\mu(i) = \mu(n) - Q(i)\mu(e^-)\,, \quad (8)$$

and

$$n(e^+) - n(e^-) + n(\mu^+) - n(\mu^-) = -\sum_i n(i)Q(i)\,, \quad (9)$$

$$\sum_i n(i) = n_B\,. \quad (10)$$

In this work, we adopt two illustrative scenarios, the first has matter with lepton fraction Y_L=0.4, trapped neutrinos and the entropy per particle S/A=1 (scenario I) and the second has neutrinoless, chemical equilibrated matter with S/A=2 (scenario II). Note that we omit the Boltzmann constant k_B because we are using natural units, in which case it assumes the value one. In the first case, consider a PNS born after the shock wave have been isolated from the collapsed material about 0.1-1 s after bounce. This is a lepton rich object with high lepton fraction due to trapped neutrinos in the core and temperature of several tens of MeV (Pons et al. (1999); Hix et al. (2003); Lentz et al. (2012)). The entropy per baryon S/A in the core is low, (Pons et al.

(1999); Hix et al. (2003); Lentz et al. (2012)), as the PNS inherited this low entropy from the progenitor star that emitted radiation during its whole lifetime.

Admittedly, both scenarios provide a rather schematic picture of the PNS birth and development. In modern CCSN simulations, all thermodynamical variables of the PNS, such as temperature, Y_L and S/A, depend on the model of the progenitor star, details of the collapse, and development of the shock, which are themselves locally dependent on the density and composition distribution of the core material, determined by a chosen EoS. However, we believe that the two examples described above provide an illustrative trend.

To facilitate better understanding of the role of microphysics in the EoS of cold and hot compact objects and providing a comparison with other models, the Chiral-Mean-Field (CMF) model and the generalized relativistic density functional with hyperons and density dependent interaction DD2 (DD2Y) were chosen. The Chiral-Mean-Field (CMF) model is based on a nonlinear realization of the SU(3) sigma model (Papazoglou et al. (1999)). It is an effective quantum relativistic model that describes hadrons and quarks interacting via meson exchange (ω, σ, ρ, δ, ϕ, and ζ). It is constructed in a chirally invariant manner, with particle masses originating from interactions with the medium and, therefore, decreasing at high densities and or temperatures. The model is in agreement with standard nuclear and astrophysical constraints (Dexheimer & Schramm (2008); Roark et al. (2019); Dexheimer et al. (2019)), as well as lattice QCD and perturbative QCD (Dexheimer & Schramm (2010); Roark & Dexheimer (2018)).

The DD2Y model (Typel (2020)) is an extension of a relativistic energy density functional with ω, σ, and ρ mesons by including the entire baryon octet and the ϕ meson. The meson-baryon couplings are assumed to depend on the total baryon density using the parametrization DD2 (Typel et al. (2010)). The hyperon couplings to the vector mesons ω, ρ and ϕ follow the scaling of the SU(6) symmetry scheme, (Weissenborn et al. (2012)). The coupling of the scalar σ-hyperon is chosen through fixing the values of the single-particle potentials in nuclear matter at saturation density.

The non-homogeneous matter below the nuclear saturation density has not been modeled in the QMC framework as yet. To cover the whole density range from the core to the surface of NS, we use the Baym-Pethick-Sunderland (BPS) (Baym et al. (1971)) EoS for the QMC and CMF models. The DD2 model already includes light and heavy clusters, as described in (Pais & Typel (2017)) below nuclear saturation density for zero and finite temperatures. We also use these finite temperature DD2 EoS to describe the crust of PNS within the QMC and CMF models. The new QMC-A EoS covers the range of temperatures from T=0 to 100 MeV, entropies per particle S/A between 0 to 6, lepton fractions from Y_L=0.0 to 0.6, and baryon number density range n_B=0.05-1.2 fm^{-3}. It also provides neutrino energies in Scenario I. The QMC-A EoS can be used in CCSN and NS merger simulations and extended beyond this range if necessary.

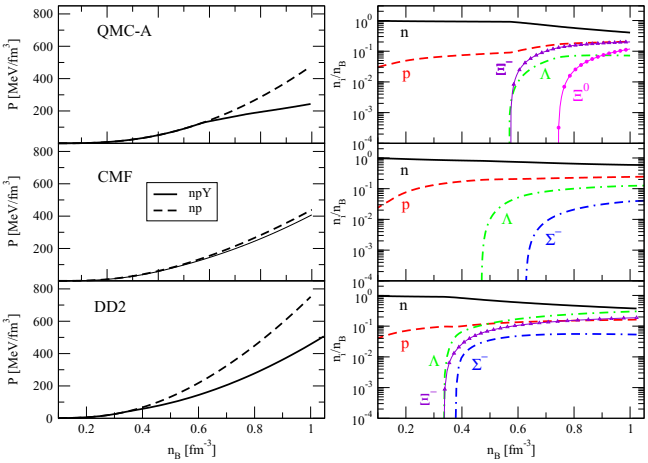

Figure 1. Equations of state of the QMC, CMF and DD2Y models at T=0 MeV. Results for the full baryon octet and nucleonic matter without hyperons are shown (left). Relative population of nucleons and hyperons in units of the total baryon number density (right). Only populations higher than 0.01% in the region of 0.1 - 1 fm^{-3} are shown.

3 RESULTS

3.1 The Equation of state and composition of high density matter

3.1.1 Cold matter

We start with application of the QMC-A model to construct an EoS for the core of cold NSs, assuming charge neutral and chemically equilibrated homogeneous matter, containing the full baryon octet, electrons and muons. In the left panels of Fig. 1, we plot the pressure dependence on the baryon number density for matter containing the entire baryon octet for the three models QMC-A, CMF, and DD2Y with the last two being used for a comparison. The density range is limited to 0.1 - 1.0 fm^{-3}, as the central densities of most cold NS models are expected to lie in this region. As anticipated, the presence of hyperons softens the EoS, leading to lowering of the slope of pressure with the onset of hyperons when compared to the pure nucleonic EoS. Different patterns of the softening are clearly related to the density distribution of hyperon population, shown in the right panels of Fig. 1 for particle fractions higher than 10^{-4}. One can easily see that the onset densities and the amount of individual species are clearly model dependent.

It is interesting to note that Abbott et al. (2018) reported a constraint on pressure at twice the nuclear saturation density to be between 11.23 and 38.7 Mev/fm^3 (with 90% confidence), derived from the analysis the GW170817 signal. Hyperons are not predicted to be present at this density in the models used in the present work. For matter composed of only nucleons, all three models predict very close values of pressure 32.99, 32.93 and 32.14 Mev/fm^3 for QMC-A, CMF and DD2Y, respectively, well within the limits extracted from the GW observation.

Examination of the right panels of Fig. 1 reveals that Λ hyperons are predicted to appear first, at threshold densities 0.5-0.6, 0.4-0.5 and 0.3-0.4 n_0, in QMC-A, CMF and DD2Y models, respectively. The other members of the full

hyperon octet, included in the models, appear at different threshold densities. The QMC-A model predicts only $\Xi^{0,-}$ hyperons, CMF shows just the Σ^- hyperon appearing at densities above 0.6 n_0 and in the DD2Y model both negatively charged hyperons, Σ^- and Ξ^-, are present at rather low densities below 0.4 n_0. The differences emerge from the differences in modeling hyperon couplings and consequent hyperon binding energies in the system.

The hyperons appear naturally at T=0 in nucleonic matter (due to the Pauli blocking) when their effective chemical potentials, increasing with density of degenerate matter, reach values above that of their effective masses. Eventually, strangeness non-conserving weak processes become possible, creating the hyperon population in the stellar core (Glendenning (1985); Balberg et al. (1999); Glendenning (2012)). The hyperon chemical potential is determined by the hyperon mass and its binding energy. This energy, arising from the hyperon-nucleon, hyperon-meson and hyperon-hyperon couplings is still poorly constrained. In QMC model the hyperon-nucleon couplings are not fitted. They are computed in the quark model, in free space as well as in matter. What is fitted in free space are the parameters of the bag model to reproduce the mass of the free octet. All the other couplings are calculated self-consistently within the model. In RMF-type models, the hyperon-meson couplings have to be fitted, usually to expected values of the potential depth for the hyperons in nuclear matter U_{YN}, constrained by (scarce) experimental data on hypernuclei (for the most recent analysis using RMF models, see (Fortin et al. (2020))). The U_{YN} potentials are *calculated* at nuclear saturation density in the QMC-A model to be U_Λ=-28 MeV, U_Σ=-0.96 MeV and U_Ξ= -12.7 MeV. In the CMF and DD2Y models the potentials are *chosen* to be U_Λ=-28 MeV, U_Σ=5.33 MeV, U_Ξ=-18.4 MeV and U_Λ=-28 MeV, U_Σ=30 MeV, U_Ξ=-14 MeV respectively. The least known coupling are the ones of the Σ hyperons.

In the QMC-A model, Σ hyperons do not appear at baryon number densities below n_B=1.0 fm^{-3} This effect was recognized already in our early work (Rikovska-Stone et al. (2007); Guichon et al. (2018)). In the QMC model, the nucleon-hyperon (N-Y) interactions are not a subject of choice, but emerge naturally from the formalism. In particular, the hyperfine interaction which splits the Λ and Σ masses in free space is significantly enhanced in-medium (Guichon et al. (2008)), leading to what is effectively a repulsive three-body force for the Σ hyperons, with no additional parameters. The absence of Σ hyperons in cold matter is supported by the fact that no bound Σ^- hypernuclei at medium or high mass has been found as yet, despite dedicated search (Harada & Hirabayashi (2006, 2015)). However, the CMF model predicts a considerable presence of Σ^- at about 4 n_0 and in the DD2Y model the Σ^- appear in the density region below 0.4 fm $^{-3}$.

The $\Xi^{0,-}$ hyperons, not predicted by the CMF model at densities below 1.0 fm^{-3}, appear in the QMC-A model at density almost identical to the threshold for Λ. Only the negative Ξ^- is observed in the DD2Y model. The presence of the Ξ hyperons at rather low densities indicates an attractive nucleon-Ξ interaction and the existence of bound Ξ^-hypernuclei. So far, two single events involving Ξ hypernuclei, ${}^{12}_{\Xi^-}$Be (Kchaustov (2000)) and ${}^{15}_{\Xi^-}$C (Nakazawa et al. (2015)), have been reported (Yoshida et al. (2019)).

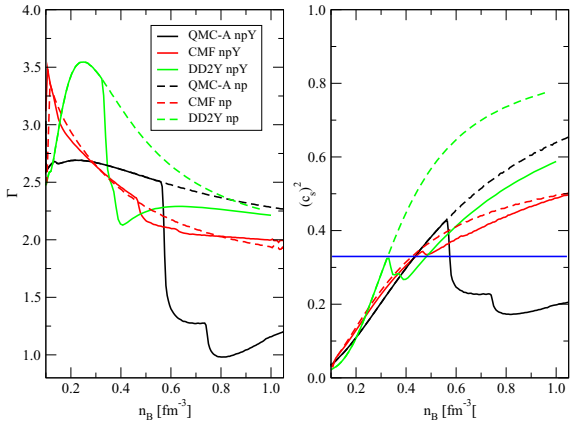

Figure 2. The adiabatic index (left) and the square of the speed of sound (right) as a function of density as computed in QMC, CMF and DD2Y models at T=0 MeV. Results for the full baryon octet and nucleonic matter without hyperons are shown. The blue horizontal line indicates the conformal limit c_s^2=1/3.

An important thermodynamic quantity closely related to the EoS is the adiabatic index Γ, a sensitive indicator of phase changes in stellar matter and the stability with respect to vibrations of a star (Akmal et al. (1998); Haensel et al. (2002); Chamel & Haensel (2008); Casali & Menezes (2010)) It is defined as

$$\Gamma = \frac{d\log P}{d\log n_B} = \frac{n_B}{P}\frac{dP}{dn_B} \ . \tag{11}$$

Polytropic EoS have constant Γ, equal to 4/3 (5/3) for a relativistic (non-relativistic) free-Fermi gas. Using realistic nucleonic EoS, Chamel & Haensel (2008) described supernova matter, with trapped neutrinos using Y_L=0.4 and S/A=1 to find that Γ was continuously growing with density, from 0.5 to 4 fm^{-3}. For multicomponent matter, Γ exhibits jumps at densities coincident with density thresholds of individual components, signaling phase transitions and/or changes in make-up of the matter.

We present in Fig. 2 the adiabatic index Γ and the speed of sound as calculated in the QMC-A, CMF and DD2Y models, in the range of density from 0.1 to 1 fm^{-3} (0.625 - 6.25 n_0), predicted to be reached in NS cores by realistic models. We see significant drops in the values of Γ at densities which are comparable with the threshold densities for appearance of hyperons (see Fig. 1). The large drop at density 0.5-0.6 fm^{-3} for QMC-A takes place because the Λ and Ξ^- hyperons appear at almost the same density. The next drop is clearly related to appearance of the Ξ^0. The CMF model shows much smaller drops at the threshold densities for the Λ^- and Σ^- hyperons. The DD2Y model predicts very close density thresholds for the Λ^- , Σ^- and Ξ^- hyperons, which can be associated with the large unresolved drop below 0.4 fm^{-3}. These bumps are manifestations of instabilities in hyperonic matter, leading to vibrations which may be damped by various processes, including bulk, viscosity before reaching equilibrium (Jones (2001b); Haensel et al. (2002); Lindblom & Owen (2002)).

The adiabatic index is closely related to the speed of

sound in units of c (here equal to 1)

$$\left(c_s\right)^2 = \frac{dP}{d\epsilon}\,, \tag{12}$$

where ϵ is the energy density. The stability and causality conditions set limits $0 \leq c_s^2 \leq 1$. Recent limits on the speed of sound derived from astrophysical observation were obtained by Bedaque & Steiner (2015) using a parameterized EoS and by Tews et al. (2018) in the framework of the chiral effective field theory. It has been argued that the speed of sound in NS matter exceeds the *conformal limit* (Cherman et al. (2009)) $c_s^2 \leq 1/3$. Very recently, Annala et al. (2020), using their pQCD model extrapolated to low densities, suggested that compliance with the conformal limit signals sizable quark-matter core in massive NS. All these studies were applied either to rather low densities or did not explicitly include hyperonic degrees of freedom. Recent discussion on the impact of irregularities in speed of sound in dense matter on the macroscopic neutron-star properties (Tan et al. (2020)) inspires more investigation along these lines.

As is demonstrated in the right panel of Fig. 2, the QMC-A model predicts a c_s^2 lower than 1/3 at densities above 0.6 fm^{-3}. The CMF and DD2Y models yield c_s^2 around 1/3 at densities between 0.3-0.5 fm^{-3}. It is not surprising that the instabilities, seen in the adiabatic index, reflect also in the density dependence of the speed of sound. In a classical analog, induced vibrations in the medium interfere with propagation of the sound wave, thus causing its impedance through the refractive index. Because the instability is larger in the QMC-A model than in the other models, the effect on the speed on the sound is more pronounced. Detailed analysis of these conjectures goes beyond the scope of this paper and will be addressed separately. However, we can rule out with certainty that the conformal behaviour of c_s^2 is a unique signature of presence of a phase transition to quark matter in the core of NS. None of the models used here has quark degrees of freedom included and yet the speed of sound is predicted to be below or close to the conformal limit. As the QMC-A, CMF and DD2Y EoS with nucleons and hyperons are in full compliance all known astrophysical constraints, Γ and c_s^2 naturally reflect these constraints.

3.1.2 *Matter at finite temperature*

We have demonstrated in the previous section that the number density dependence of the thresholds for the appearance of hyperons in dense matter and their population in cold stars are model dependent. This model dependence is still more apparent at finite temperatures, where the temperature effects smear out the density thresholds for appearance of hyperons, thus, appearing at low density and, consequently, within the cores of warm low mass NS. The population distribution of nucleons and hyperons at the two scenarios adopted in this work, are presented in Fig. 3. Comparing Fig. 1 and Fig. 3 indicates an increase of hyperonic content in scenario I, followed by a more dramatic increase in scenario II. In the latter, population of the entire octet in fractions larger than 10^{-4} is predicted by all three models at densities below the respective thresholds at T=0 MeV. The presence of neutrinos and somewhat lower temperature (see Fig. 4) inhibits, to some extent, the creation of hyperons in scenario I.

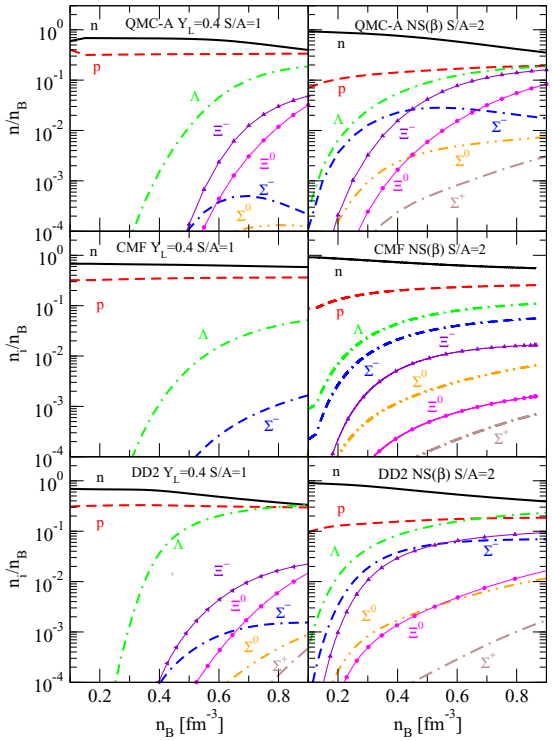

Figure 3. The same is Fig. 1 but for in scenario I (left) and scenario II (right). Only populations higher than 0.01% in the region of baryon density between 0.1 - 1 fm^{-3} are shown.

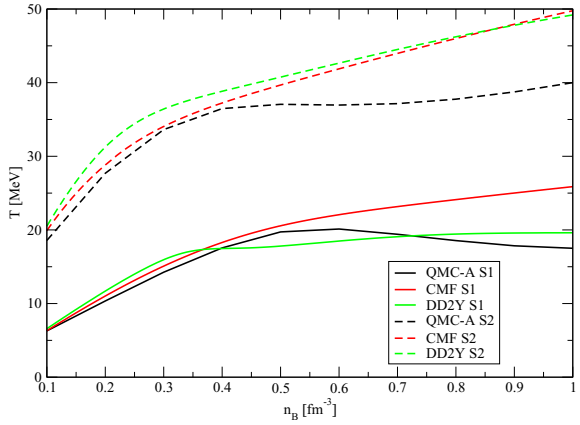

Figure 4. Temperature distribution as a function of baryon density in scenarios I and II (denoted as S1 and S2).

The temperature effect on the adiabatic index and the speed of sound at finite temperature is illustrated in Fig. 5. We observe a much smoother density dependence of Γ, reflecting the absence of the thresholds present in the T=0 MeV case. In the QMC-A model, the speed of sound is almost constant below 1/3 in scenario II and in scenario I it remains below 0.4, again not showing the dependence on

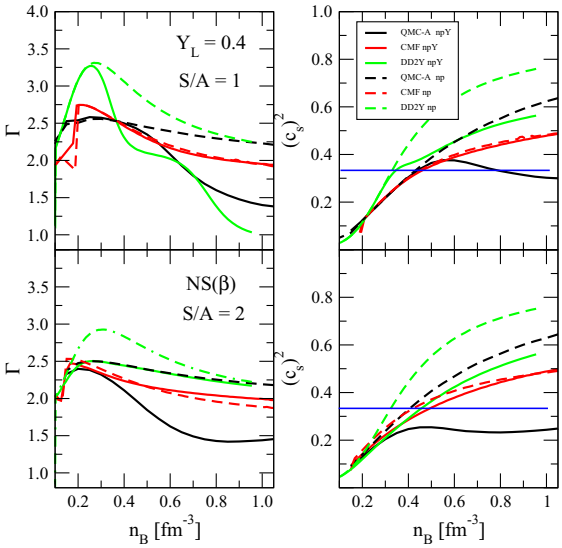

Figure 5. The same as Fig. 2 but for scenarios I and II.

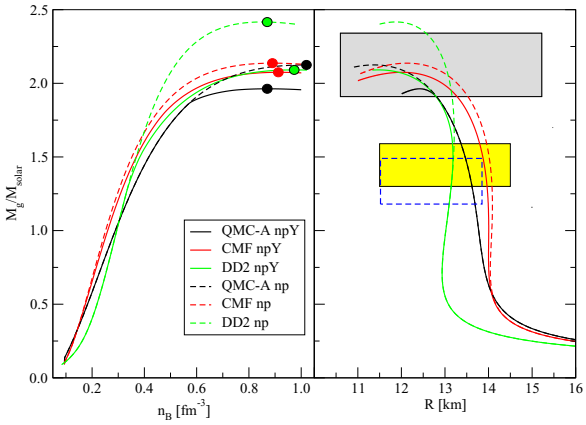

Figure 6. Neutron star masses as a function of the central baryon density (left) and radius (right) computed with the QMC-A, CMF and DD2Y models for hyperonic (solid line) and nucleonic (dashed) matter. Observational limits on the maximum mass configuration and its radius are illustrated by the grey rectangle. Recent observation from the NICER mission limiting mass and radius of a ~1.4 $M_\odot$ of PSR J0030-0451, analysed independently by Miller et al. (2019) (yellow rectangle) and by Riley et al. (2019) (blue dashed contour) are added for completeness. The colored full circles in the left panel indicate the maximum masses.

the increasing population of hyperons with growing density demonstrated in Fig 3. In CMF and DD2Y models there is a very little difference between the density dependence of the speed of sound in scenarios I and II, showing a smooth growth up to the value of about 0.6 at density 1.0 fm^{-3}.

3.2 Neutron star masses and radii

3.2.1 Cold neutron stars

In the multimesenger era, when not only data on masses and radii of NS are accumulating and becoming more precise, but also the analysis of the GW signals is continuously providing additional constraints, the choice of the EoS of the NS interior narrows. We use all this information to investigate cold NS models built using the QMC-A, CMF and DD2Y EoS. First, the TOV equation (Tolman (1939); Oppenheimer & Volkoff (1939)) is solved to yield the gravitational mass and radius of a non-rotating, spherically symmetric cold NS. The computed gravitational masses as a function of radii (right panel) and of the central baryonic density (left panel) are shown Fig. 6.

Our results are compared with the most recent data from observation. Cromartie et al. (2019) reported gravitation mass of the J0740+6620 millisecond pulsar, obtained combining data from NANOGrav and the Green Bank telescope, to be $2.14^{+0.20}_{-0.18}$ $M_\odot$ with 95.4% credibility interval and $2.14^{+0.10}_{-0.09}$ $M_\odot$ with 68.3% credibility interval. Antoniadis et al. (2013) studied the PSR J0348+0432 neutron star-white dwarf systems and derived the pulsar mass as 2.01±0.04 $M_\odot$.

Further observation of the binary millisecond pulsar PSR J1614-2230, reduced the original results, 1.97±0.04 $M_\odot$ to 1.928±0.017 (Fonseca et al. (2016)). We adopt the range of gravitational masses from observation, including their uncertainty, from 1.91 to 2.34 $M_\odot$ in the right panel of Fig. 6. Complementary to those measurements, Rezzolla et al. (2018), combining the GW observations of merging systems of binary NS and quasi-universal relations, set constraints on the maximum mass that can be attained by non-rotating stellar models of NS, implying that the maximum mass of a non-rotating NS is between $2.01^{+0.04}_{-0.04}$ and $2.16^{+0.17}_{-0.15}$ $M_\odot$. The QMC-A, CMF and DD2Y models with hyperons produce NS with the maximum gravitational mass consistent within these limits. The maximum mass of a purely nucleonic NS lies within the observational limits for the QMC-A and CMF EoS, but is somewhat higher for the DD2Y EoS.

The deduction of stellar radii for the maximal mass configuration from observation is rather involved. There are many estimates in the literature (see e.g. Özel & Freire (2016)), but the constraints they provide are still rather wide, 10 - 15 km, as a simultaneous observation of a heavy NS and its radius has not been yet achieved. The much needed information for constraining the theory is complicated because the TOV equation yields only the gravitational mass of a NS as a function of its radius. Recent GW observation directed the attention to lower-mass stars, with masses around the canonical value of 1.4 $M_\odot$. However, the GW data supply only information on masses and tidal deformation. Constraints on radii have to be inferred, often in combination with data from electromagnetic observation, in a model dependent way (Abbott et al. (2018); Raithel (2019); Weih et al. (2019)). Note that even when using universal relations to obtain stellar radii (Yagi & Yunes (2013); Chatziioannou et al. (2018); Abbott et al. (2018) the equation of state dependency cannot be fully eliminated.

Steiner et al. (2013) derived that the radius of a 1.4 $M_\odot$ star, $R_{1.4}$, should lie between 10.4 and 12.9 km from data on transiently accreting and bursting low mass X-ray binaries sources, independent of the structure of the core. The up-

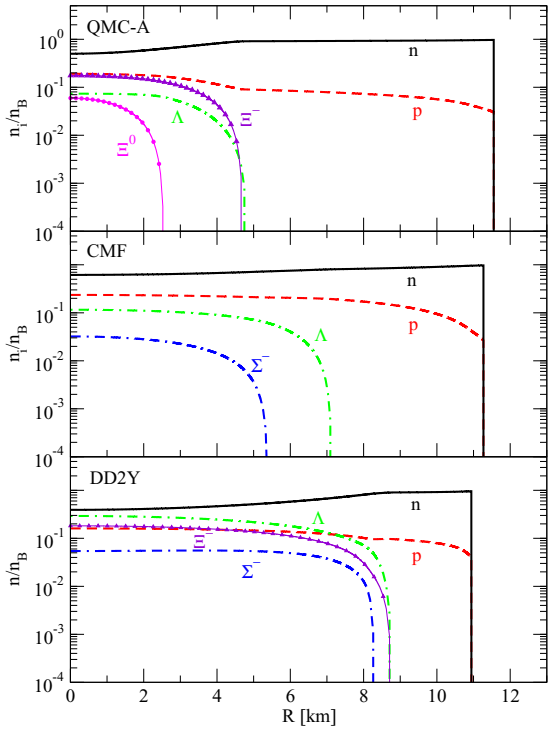

Figure 7. Particle number densities normalized to the total baryon density as function of stellar radius of the most massive neutron star. Only populations higher than 0.01% are shown.

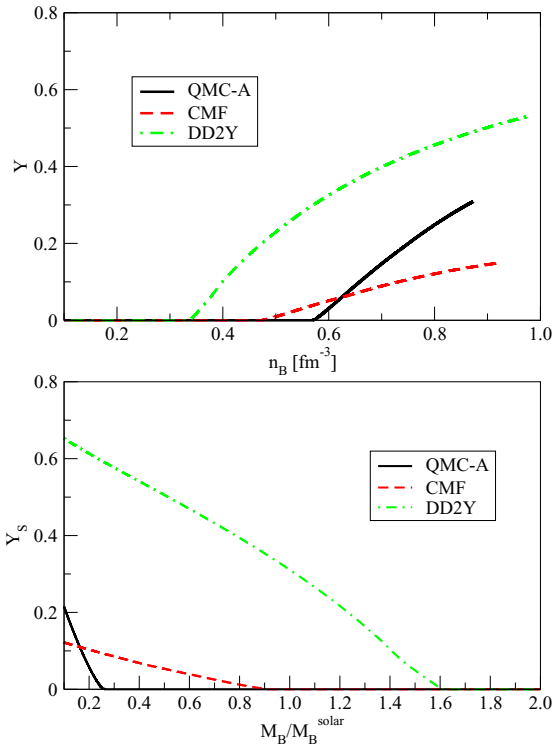

Figure 8. Total hyperon fraction as a function of baryon number density as calculated in the QMC-A, CMF and DD2Y models at T=0 MeV (top panel) and the total strangeness fraction in the enclosed neutron-star baryonic mass (bottom panel).

.

per limit on $R_{1.4}$ was found to be 13.6 km by Annala et al. (2018), who used a piece-wise polytropic EoS, compatible at high densities with pQCD and using the GW limits on tidal deformability. Burgio et al. (2019) translated the limits on average tidal deformability, imposed by the GW signal, into limits on the $R_{1.5}$ to be 11.8 km and of a $\sim R_{1.4}$ to be $\sim$ 13.1 km. Raithel (2019) obtained limits on the $R_{1.4}$ to be 9.8 - 13.2 km from Bayesian analysis of the GW data. Recently, Capano et al. (2020) constructed a large number of EoS using effective field theory and marginalized them using the GW observations. They obtained $R_{1.4}=11.0^{+0.9}_{-0.6}$ km (90% credibility interval), with the upper limit lower than the one of Burgio at al. Very recently, Al-Mamun et al. (2020) combined electromagnetic and gravitational wave constraints in a Bayesian analysis and obtained a set of 1σ and 2σ constraints on $R_{1.4}$ with mean points around 12 km. But note that all these limits are, at least to certain extend, dependent on the EoS used in the analysis (see e.g. Dexheimer et al. (2019)) for a study showing that, even within one model, considering different nuclear interactions can change the radius-tidal deformation relation.

The only observational data known to us which report gravitational mass and the corresponding radius on the same object are the results from the NICER mission. Bayesian inference approach of the energy-dependent thermal X-ray waveform of the isolated 205.53 Hz millisecond pulsar PSR J0030+0451 yields its estimated mass $1.44^{+0.15}_{-0.14}$ $M_\odot$ and radius $13.02^{+1.24}_{-1.06}$ km with 68% confidence level Miller et al. (2019), consistent with the outcome of an independent analysis by Riley et al. (2019) $1.34^{+0.15}_{-0.16}$ $M_\odot$ and radius $12.71^{+1.14}_{-1.19}$ km. We display these data in the right panel of Fig. 6.

Lattimer & Prakash (2005) proposed that EoS-independent Tolman VII solution to Einstein's equations sets an upper limit to the central density of cold, non-rotating NS with maximum mass configurations between 1.8 - 2.1 $M_\odot$ in the range 9 - 10 n_B/n_0 (see Fig.1 in Lattimer & Prakash (2005)). All three models in this work are well within this limit with central densities 4.75, 5.69 and 5.87 n_B/n_0 for QMC-A, CMF and DD2Y models, respectively, as demonstrated in the left panel of 6.

It is interesting to note that this central density seems to be rather independent of the hyperonic core make up. Density distributions of nucleons and hyperons in configurations with maximum masses as function of stellar radius are illustrated in Fig. 7 (for the core only). A significant difference in hyperon populations in the three models, the QMC and the CMF, when compared to the DD2 model, is apparent. The large increase in strangeness population reflects mainly in the lowering of the maximum mass in the DD2Y model, but also other differences between the nucleonic and hyperonic stars predicted in the QMC and CMF models.

Fig. 7 shows that the radial distribution of particle species in a cold star is again model dependent. All hyperon species disappear at roughly 5, 7, and 9 km from the stellar center in the QMC-A, CMF and DD2Y mod-

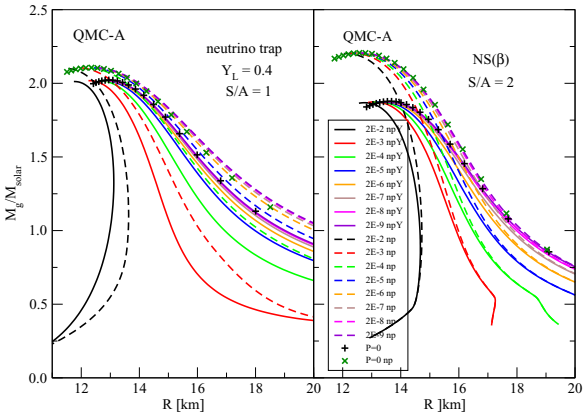

Figure 9. Illustration of the search for the surface of a hot PNS in scenario I (left panel) and scenario II (right panel), as calculated in the QMC-A model. Only results for n_B in the region 2.0×10^{-2} - 2.0×10^{-9} fm^{-3} are shown for clarity.

els, respectively. Beyond these thresholds, the NS matter is composed only of nucleons and leptons (not shown here). The hyperon content in the PNS can be further quantified by examination of the total hyperon fraction $Y=\sum_j n(j)/n_B$ and total strangeness fraction $Y_s=\sum_j S(j)n(j)/n_B$, where j denotes a hyperonic specie and S the strangeness number. The baryon number density dependence of the hyperon fraction (top panel) and the fraction of strange matter in a star with a given baryon mass (bottom panel) are illustrated in Fig. 8 . They show how hyperons dominate the behaviour of a massive NS within the DD2Y model and the behaviour of their inner cores within the QMC model.

3.2.2 Neutron stars at finite temperatures (PNS)

Calculation of the structure of a hot PNS is complicated by the uncertainty in the location of the neutrinosphere, which is needed as a boundary condition for solution of the TOV equation. We have examined the dependence of the maximum mass and the corresponding radius by solving the TOV equation up to a fixed baryon number density in the region of 2.0×10^{-2} - 2.0×10^{-12} fm^{-3}, instead of locating the surface of the star at zero pressure. The results, shown in Fig. 9, demonstrate that the maximum gravitational mass and the corresponding radius, computed at surface density lower than $n_B \leq 2.0\times^{-9}$ fm^{-3} are practically identical to those obtained with the definition of the surface at zero pressure. This conclusion holds for all scenarios and the EoS considered in this work. We observed a minor difference in radii of the lower mass models for the case of neutrino trapping matter, which is likely reflecting the accuracy of the calculation at very low particle number density. The study was repeated for the CMF and DD2Y models with very similar results. We have adopted 2.0×10^{-12} fm^{-3} as the surface density in all cases.

The properties of hot stars as calculated here are summarized in Table 1 in comparison with the T=0 results. Finite temperature changes significantly the distribution of hyperons inside a PNS, when compared to a cold star. We have already shown in Sec. 3.1.2 that the population of hyperons grows with increasing density and temperature. In Fig. 10 we demonstrated that radial distribution of the hyperon population inside the stellar core is also significantly impacted, contrary to the result at zero temperature, by increasing temperature. Comparing Fig. 7 with Fig. 10 shows that, for example, Λ hyperons can be found almost throughout the whole volume of massive stars, reaching close to 10 km from the stellar center. This spreading is wider in scenario II, in which the PNS is hotter than in scenario I.

Table 1. Macroscopic properties of stars, as predicted in the QMC-A, CMF and DD2Y models in different scenarios. Gravitational mass in units of $M_\odot$, radius in km, central pressure P and energy density ϵ in MeV/fm^3, and central baryonic density n_B in fm^{-3} for different stars, scenarios and composition. The value of the slope of the symmetry energy at saturation L in MeV in cold, nucleon only matter is added in connection with the radius of the 1.4 $M_\odot$ NS. For more discussion see text.

Model	QMC-A	CMF	DD2Y
NS hyperons			
M_{max}	1.963	2.075	2.091
R	12.42	12.04	11.47
P_{cent}	210.7	337.4	435.1
ϵ_{cent}	1005	1111	1221
$n_{B_{cent}}$	0.872	0.908	0.973
NS nucleons			
M_{max}	2.125	2.137	2.417
R	11.37	12.16	11.87
P_{cent}	502.8	352.3	519.4
ϵ_{cent}	1273	1085	1099
$n_{B_{cent}}$	1.019	0.892	0.851
$R_{1.4}$	13.55	14.14	13.17
L	54	88	58
P_{cent}	45.9	56.8	46.8
ϵ_{cent}	387.7	329.0	353.3
$n_{B_{cent}}$	0.388	0.328	0.353
PNS hyperons scenario I			
M_{max}	2.022	2.025	2.177
R	12.987	12.51	12.46
P_{cent}	256.5	369.1	414.0
ϵ_{cent}	1122	1208	1143
$n_{B_{cent}}$	0.880	0.937	0.883
PNS nucleons scenario I			
M_{max}	2.107	2.041	2.372
R	12.40	12.69	12.3
P_{cent}	410.0	376.7	590.6
ϵ_{cent}	1237	1197	1139
$n_{B_{cent}}$	0.940	0.929	0.844
PNS hyperons scenario II			
M_{max}	1.966	2.077	2.068
R	13.61	12.57	12.08
P_{cent}	181.8	317.6	428.9
ϵ_{cent}	956.9	1075	1248
$n_{B_{cent}}$	0.815	0.862	0.963
PNS nucleons scenario II			
M_{max}	2.205	2.203	2.426
R	12.65	13.5	12.79
P_{cent}	329.8	343.0	463.8
ϵ_{cent}	1111	978.4	1039
$n_{B_{cent}}$	0.874	0.783	0.789

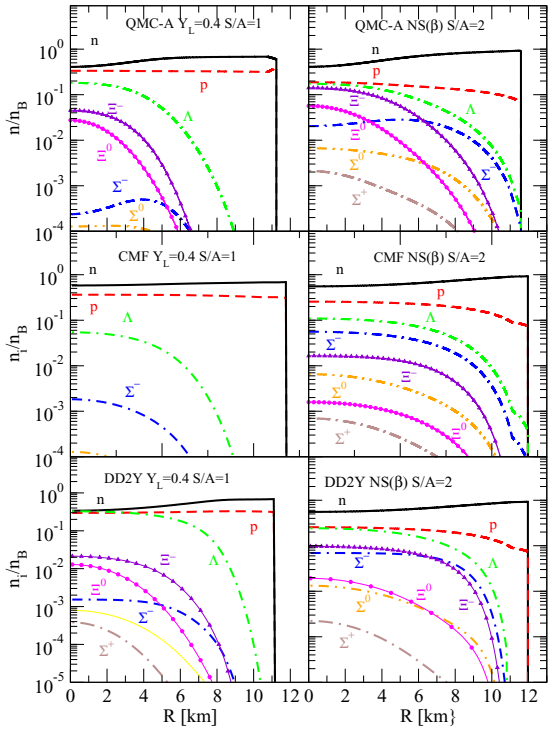

Figure 10. The same as Fig. 7 but for hot PNS in scenario I and II.

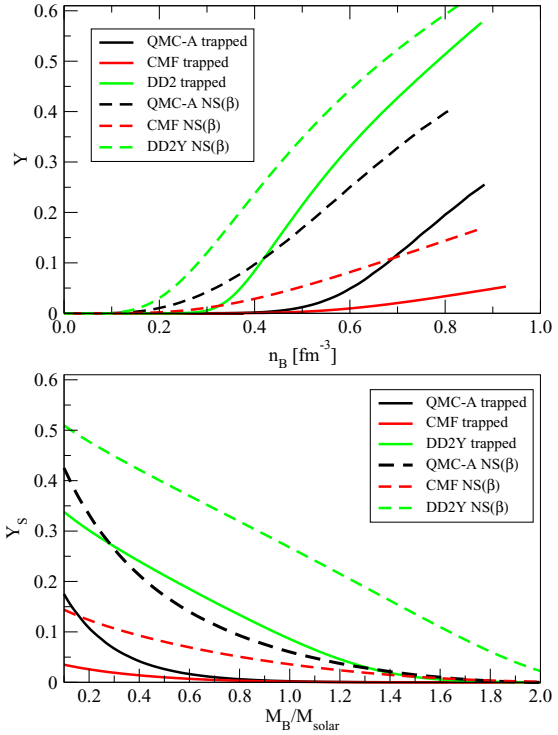

Figure 11. Total hyperon fraction as a function of baryon number density as calculated in the QMC-A, CMF and DD2Y models (top panel) and the total strangeness fraction in the enclosed neutron-star baryonic mass (bottom panel) at finite temperature in scenarios I and II for a comparison with Fig. 8 .

It has been suggested (Lopes & Menezes (2014); Hu et al. (2020); Li & Magno (2020)) that there is a correlation between the slope of the symmetry energy, L, and the radius of the canonical 1.4 $M_\odot$ NS. We find (see Table 1) that this correlation is not strong in the cases studied in this paper. Although the CMF model predicts L=88 MeV and the radius $R_{1.4}$ = 14.14 km and both QMC-A and DD2 models have smaller value of L, 54 MeV and 58 MeV, and smaller radii, 13.55 km and 13.17 km, respectively, the relation between predictions of the QMC-A and DD2 models is reversed.

In the same fashion, the total hyperon fraction and strangeness fraction in both scenarios I and II, displayed in Fig. 11, predict a substantial amount of strangeness present in a PNS just a few milliseconds after birth. This amount decreases during the cooling process when some strangeness producing reactions freeze out and the composition of the NS core is fixed to what is expected in cold stars (see Fig. 1).

4 ROTATING STARS

So far, we have investigated properties of cold and hot static NS. Now, we turn our attention to rigid rotation (differential rotation goes beyond the scope of the present manuscript), which deepens our discussion, as it affects not only the masses and radii of stars, but also their composition in a significant way. It is still an open question whether PNS rotate at their birth, but there is significant evidence of, for example, fast rotating young millisecond pulsars (Bassa et al. (2017); Pleunis et al. (2017)). It is not clear whether a star in a close binary system can gain angular momentum just before merging. But if it can, the calculation of its mass may be different. The data on dynamics of the stars should be added to the prior in a Bayesian treatment.

Let us start our discussion with the moment of inertia I, which is a candidate for providing a much needed observational constraint of the high density EoS. It is proportional (using Newtonian physics for simplicity in this argument) to the mass M of a star times its radius R squared. Thus, if the mass of a star is known, its radius can be determined from observation of its moment of inertia. Together with the quadrupole moment, Q, and the Love number, k_2, reflecting the deviation from sphericity and the deformability of the star, I is one of the global observables which is believed to exhibit universal relations (see Wei et al. (2019) and references therein), which are approximately equation of state independent.

Here we calculate two quantities, I/M^3, and I/MR^2, as a function of the stellar gravitational mass and its compactness, M/R. The results are shown for cold (hot) stars in Fig. 12 (Fig. 13), confirming that the three models analyzed in this work, QMC-A, CMF, and DD2Y, indeed exhibit very similar patterns for these quantities, thus, being good candidates to be included in data sets leading to extraction of the most likely value of stellar radius from a known mass and moment of inertia. Note that the EoS spread seen in Fig. 13

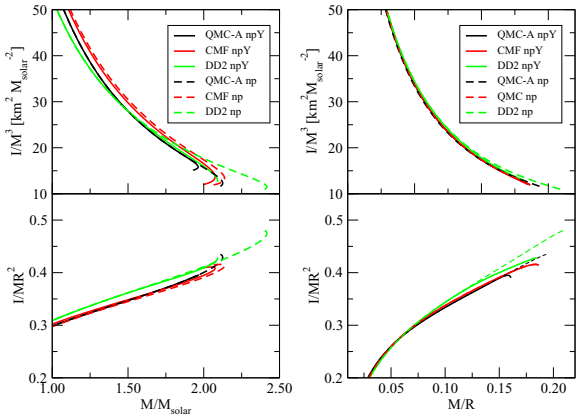

Figure 12. The normalized moment of inertia I/M^3 (top) and I/MR^2 (bottom) vs. gravitational mass (left) and compactness M/R (right) calculated for T=0 MeV. Note that the figure is organized at the same way as Figure 2 in (Wei et al. (2019)) to allow for a comparison of EoS.

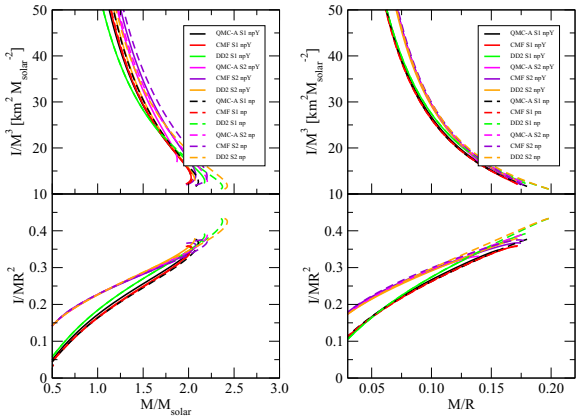

Figure 13. The same as Fig. 12 but for hot PNS stars in scenarios I and II.

is expected to be larger at finite temperature Martinon et al. (2014). In particular, there is a systematic difference between the curves for scenario I and scenario II. Further exploration of universal relations between global parameters of NS is in progress.

This calculation was performed using a slow rotation code based on the Hartle-Thorne method (Miller (2020)) It is, however, also interesting to explore fast rotating stars close to and at their Kepler frequency, the maximum frequency at which stars are still compact, not shedding matter. In particular, the limit on the maximum mass of a fast spinning star is important for the ongoing discussion of the possible identification of the compact object with a gravitational mass around 2.6 $M_\odot$, recently observed though the detection of gravitational waves from its merger GW190814, as a neutron star (Abbott et al. (2020); Dexheimer et al. (2020)). For this purpose, we used the publicly available RNS code (Stergioulas & Friedman (1995)).

In Fig. 14, we show gravitational masses for cold (top-left panel) and warm (top-right panel) stars rotating at the Kepler frequency. It can be seen that nucleonic stars can carry gravitational masses up to 2.5 - 2.7 $M_\odot$, but hyperonic stars can only carry gravitational masses up to 2.3 - 2.5 $M_\odot$ for the different models. Therefore the compact object with 2.6 $M_\odot$ may not be out of the question as a neutron star if it rotates close to the Kepler frequency, identified in the bottom-left panel. It is also interesting to see limiting rotation frequencies for low mass NS, relevant for BNSM, where the spread is not large. This is not the case for PNS, where the mass and Kepler frequency spread is large for a given (small or large) central energy density. We are aware of the fact that hot PNS are less compact and therefore may rotate faster than cold stars. However, the results in Fig. 14 suggest the opposite trend. This may be an effect of the larger hyperon content spread out all over the core or, possibly, of just using only rigid rotation model. We will investigate the rotation patterns of hot stars in more detail in future work.

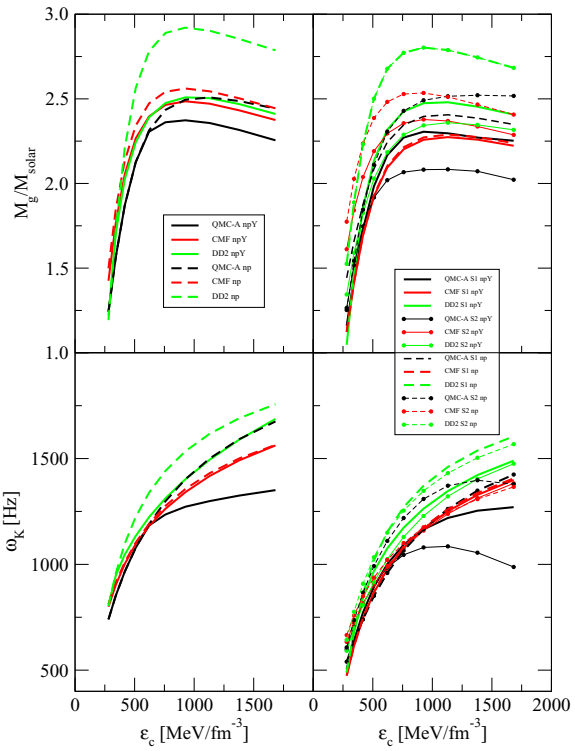

Figure 14. Gravitational mass (top) and the Kepler frequency (bottom) vs central energy density for cold stars (left) and hot stars (right).

5 SUMMARY AND OUTLOOK

In this work, we presented for the first time results for the QMC-A model, based on sub-nucleon degrees of freedom, for conditions modeled after different stages of stellar evolution, including one for neutron stars and two different stages for proto-neutron stars. The latter included a lower constant entropy per baryon together with a large amount of leptons (including neutrinos) and a larger constant entropy per

baryon free of neutrinos. These two different stages inspired by supernova explosion simulations provided us with a temperature distribution that modified the particle population content in stars. In all cases, a substantial amount of hyperons were found in the core of massive stars, although larger in the first two evolution stages than in the later one, signaling how strangeness changes over time. Note that the slightly lower amount of hyperons in the first stage considered to model proto-neutron stars comes from the imposition of fixed lepton fraction.

The hyperon population reflects on the maximum possible stellar mass found in different states of evolution, which decreases with time. Of course, as expected, if the hyperons are artificially suppressed, stellar masses increase for any given stage condition. But there is no motivation to do so, as hyperons naturally appear in dense matter as soon as the Fermi energy of the system is larger than the respective hyperon chemical potential (at zero temperature), which depends not only on its mass, but also on the interactions. The QMC-A model has very few coupling parameters, which are constrained in order to fulfill nuclear constraints, including radii derived from tidal deformability of low mass cold stars. This formalism predicts, for example, that no Σ hyperons appear in cold neutron stars, which is backed up by the absence of measured Σ hypernuclei.

In this work, we have also shown the effect of the appearance of hyperons in the adiabatic index and in the speed of sound c_S. We found that a low speed of sound within the conformal limit at large densities $c_S^2 < 1/3$ can be reproduced by our hadronic model, not being in this case a unique fingerprint of quark matter cores in neutron stars, but more a general consequence of instabilities caused by a (not first-order) phase transition, such as from nucleonic to hyperonic matter. Our results re-open the question of the existence of r-modes in rotating neutron stars (Andersson & Kokkotas (2001); Haskell (2015)). Jones (2001b,a) reported that the bulk viscosity of hyperonic matter in neutron stars would produce a serious damping of the r-modes. Lidblom and Owen Lindblom & Owen (2002) argued that although the cooling of the PNS is too rapid to influence the r-modes. It will be interesting to pursue the connection between r-modes and the internal composition of neutron stars in the future.

When rotation is included, our moment of inertia relations follow the standard universal relations determined by other models. We can also reproduce massive stars, such as the neutron-star candidate observed in the gravitational-wave merger event GW190814 when rotation frequencies were taken to the Kepler limit. For this purpose, we used the publicly available RNS code.

Throughout this work, we compared our results with results from two other relativistic models, the DD2 and the CMF, each one containing very different physics. In this way, we could have a better idea of how model dependent our results were. To build our figures and table, we have constructed QMC-A equation of state tables containing data in the parameter space compatible with core-collapse supernovae and neutron star mergers simulations. These tables will be posted on the CompOSE depository (http://compose.obspm.fr) in the near future.

ACKNOWLEDGMENTS

We are indebted to John Miller for suppling some of the essential software for analysis of the model data and many elucidating discussions and to Stefan Typel for supplying the DD2(DD2Y) EoS prior to publication and valuable comments. JRS and PAMG acknowledge a fruitful discussion with Andrew Steiner during the course of writing the computer code used in this work and hospitality during their stay at the University of Adelaide. This work was supported by the University of Adelaide and the Australian Research Council through the ARC Centre of Excellence in Particle Physics at the Terascale (CE110001004) and grants DP180100497 and DP150103101. VD is supported by the National Science Foundation under grant PHY-1748621.

REFERENCES

Abbott B., et al., 2017, Physical Review Letters, 119
Abbott B., et al., 2018, Physical Review Letters, 121
Abbott R., et al., 2020, Astrophys. J. Lett., 896, L44
Akmal A., Pandharipande V. R., Ravenhall D. G., 1998, Physical Review C, 58, 1804
Al-Mamun M., et al., 2020, arXiv:2008.12817
Andersson N., Kokkotas K. D., 2001, International Journal of Modern Physics D, 10, 381
Annala E., Gorda T., Kurkela A., Vuorinen A., 2018, Physical Review Letters, 120
Annala E., Gorda T., Kurkela A., Nättilä J., Vuorinen A., 2020, Nature Physics
Antoniadis J., et al., 2013, Science, 340, 6131
Baiotti L., Rezzolla L., 2017, Reports on Progress in Physics, 80, 096901
Balberg S., Lichtenstadt I., Cook G. B., 1999, The Astrophysical Journal Supplement Series, 121, 515
Banik S., Char P., 2014, DAE Symp. Nucl. Phys., 59, 822
Bassa C. G., et al., 2017, Astrophys. J., 846, L20
Bauswein A., Bastian N.-U. F., Blaschke D. B., Chatziioannou K., Clark J. A., Fischer T., Oertel M., 2019, Physical Review Letters, 122
Baym G., Pethick C., Sutherland P., 1971, The Astrophysical Journal, 170, 299
Bedaque P., Steiner A. W., 2015, Physical Review Letters, 114
Burgio G. F., Schulze H. J., Li A., 2011, Phys. Rev.C, C 83, 025804
Burgio G., Schulze H.-J., Wei J.-B., 2019, Nuclear and Particle Physics Proceedings, 306-308, 61
Burrows A., Lattimer J. M., 1986, Astrophys. J., 307, 178
Burrows A., Mazurek T. J., Lattimer J. M., 1981, The Astrophysical Journal, 251, 325
Camelio G., Lovato A., Gualtieri L., Benhar O., Pons J. A., Ferrari V., 2017, Phys. Rev., D96, 043015
Capano C. D., et al., 2020, Nature Astronomy
Casali R. H., Menezes D. P., 2010, Brazilian Journal of Physics, 40
Chamel N., Haensel P., 2008, Living Reviews in Relativity, 11, 10
Chatterjee D., Vidaña I., 2016, The European Physical Journal A, 52
Chatziioannou K., Haster C.-J., Zimmerman A., 2018, Phys. Rev. D, 97, 104036
Cherman A., Cohen T. D., Nellore A., 2009, Physical Review D, 80
Cromartie H. T., et al., 2019, Nature Astronomy
Demorest P., Pennucci T., Ransom S., Roberts M., Hessels J., 2010, Nature, 467, 1081
Dexheimer V., Schramm S., 2008, Astrophys. J., 683, 943

Dexheimer V., Schramm S., 2010, Phys. Rev. C, 81, 045201
Dexheimer V., de Oliveira Gomes R., Schramm S., Pais H., 2019, J. Phys. G, 46, 034002
Dexheimer V., Gomes R., Klähn T., Han S., Salinas M., 2020, arXiv:2007.08493v1
Ferrari V., Miniutti G., Pons J. A., 2003, Monthly Notices of the Royal Astronomical Society, 342, 629
Fonseca E., et al., 2016, The Astrophysical Journal, 832, 167
Fortin M., Raduta A. R., Avancini S., Providência C., 2020, Physical Review D, 101
Fujimoto Y., Fukushima K., Murase K., 2018, Physical Review D, 98
Fujimoto Y., Fukushima K., Murase K., 2020, Physical Review D, 101
Glendenning N. K., 1985, Astrophys. J., 293, 470
Glendenning N. K., 2012, Compact stars: Nuclear physics, particle physics and general relativity. Springer Science & Business Media
Goussard J.-O., Haensel P., Zdunik J. L., 1998, Astron. Astrophys., 330, 1005
Greif S. K., Raaijmakers G., Hebeler K., Schwenk A., Watts A. L., 2019, Monthly Notices of the Royal Astronomical Society, 485, 5363
Guichon P. A. M., 1988, Phys. Lett., B200, 235
Guichon P. A. M., Saito K., Rodionov E. N., Thomas A. W., 1996, Nucl. Phys., A601, 349
Guichon P. A. M., Thomas A. W., Tsushima K., 2008, Nucl. Phys., A814, 66
Guichon P. A. M., Stone J. R., Thomas A. W., 2018, Prog. Part. Nucl. Phys., 100, 262
Haensel P., Levenfish K. P., Yakovlev D. G., 2002, Astronomy & Astrophysics, 394, 213
Harada T., Hirabayashi Y., 2006, Nucl. Phys. A, 767, 206
Harada T., Hirabayashi Y., 2015, Phys. Lett., B740, 312
Haskell B., 2015, International Journal of Modern Physics E, 24, 1541007
Hix W. R., Mezzacappa A., Messer O. E. B., Bruenn S. W., 2003, J. Phys., G29, 2523
Horowitz C. J., et al., 2014, J. Phys., G41, 093001
Hu J., Bao S., Zhang Y., Nakazato K., Sumiyoshi K., Shen H., 2020, arXiv:2002.00562v1
Ishizuka C., Ohnishi A., Tsubakihara K., Sumiyoshi K., Yamada S., 2008, Journal of Physics G: Nuclear and Particle Physics, 35, 085201
Jones P. B., 2001a, Physical Review D, 64, 084003
Jones P. B., 2001b, Physical Review Letters, 86, 1384
Kchaustov P., 2000, Physical Review C, 61, 054603
Lattimer J. M., Douglas Swesty F., 1991, Nuclear Physics A, 535, 331
Lattimer J. M., Prakash M., 2005, Physical Review Letters, 94
Lentz E. J., Mezzacappa A., Messer O. E. B., Hix W. R., Bruenn S. W., 2012, The Astrophysical Journal, 760, 94
Li B.-A., Magno M., 2020, arXiv:2008.11338v1
Lim Y., Holt J. W., 2019, The European Physical Journal A, 55
Lindblom L., 2018, Physical Review D, 97
Lindblom L., Owen B. J., 2002, Physical Review D, 65, 063006
Lindblom L., Owen B. J., 2020, Physical Review D, 101
Lopes L. L., Menezes D. P., 2014, Brazilian Journal of Physics, 44, 774
Malfatti G., Orsaria M. G., Contrera G. A., Weber F., IRanea-Sandoval I. F., 2019, Physical Review C, 100, 515
Marques M., Oertel M., Hempel M., Novak J., 2017, Phys. Rev., C96, 045806
Martinez K. L., Thomas A. W., Stone J. R., Guichon P. A. M., 2019, Physical Review C, 100
Martinez K. L., Thomas A. W., Guichon P. A. M., Stone J. R., 2020, Physical Review C, 102
Martinon G., Maselli A., Gualtieri L., Ferrari V., 2014, Phys. Rev. D, 90, 064026
Mena-Fernández J., González-Romero L. M., 2019, Physical Review D, 99
Miller J., 2020, private communication, unpublished
Miller M. C., et al., 2019, The Astrophysical Journal, 887, L24
Mishra A., Kumar A., Sanyal S., Dexheimer V., Schramm S., 2010, The European Physical Journal A, 45, 169
Most E. R., Jens Papenfort L., Dexheimer V., Hanauske M., Stoecker H., Rezzolla L., 2020, Eur. Phys. J. A, 56, 59
Nakazawa K., et al., 2015, PTEP, 2015, 033D02
Nättilä J., Steiner A. W., Kajava J. J. E., Suleimanov V. F., Poutanen J., 2016, Astronomy & Astrophysics, 591, A25
Oertel M., Fantina A. F., Novak J., 2012, Phys. Rev.C, 85, 055806
Oertel M., Gulminelli F., Providência C., Raduta A. R., 2016, The European Physical Journal A, 52
Oertel M., Hempel M., Klähn T., Typel S., 2017, Rev. Mod. Phys., 89, 015007
Oppenheimer J. R., Volkoff G. M., 1939, Physical Review, 55, 374
Özel F., Freire P., 2016, Annual Review of Astronomy and Astrophysics, 54, 401
Pais H., Typel S., 2017, in , Nuclear Particle Correlations and Cluster Physics. WORLD SCIENTIFIC, pp 95–132, doi:10.1142/9789813209350_0004
Panda P. K., Providencia C., Menezes D. P., 2010, Phys. Rev.C, 82, 045801
Papazoglou P., Zschiesche D., Schramm S., Schaffner-Bielich J., Stoecker H., Greiner W., 1999, Phys. Rev. C, 59, 411
Pleunis Z., et al., 2017, Astrophys. J., 846, L19
Pons J. A., Reddy S., Prakash M., Lattimer J. M., Miralles J. A., 1999, Astrophys.J., 513, 780
Pons J. A., Steiner A. W., Prakash M., Lattimer J. M., 2001, Physical Review Letters, 86, 5223
Prakash M., Bombaci I., Prakash M., Ellis P. J., Lattimer J. M., Knorren R., 1997, Physics Reports, 280, 1
Raaijmakers G., Riley T. E., Watts A. L., 2018, Monthly Notices of the Royal Astronomical Society, 478, 2177
Raithel C. A., 2019, Eur. Phys. J. A, 55, 80
Rezzolla L., Most E. R., Weih L. R., 2018, Astrophys. J., 852, L25
Rikovska-Stone J., Guichon P. A. M., Matevosyan H. H., Thomas A. W., 2007, Nucl. Phys., A792, 341
Riley T. E., et al., 2019, The Astrophysical Journal, 887, L21
Roark J., Dexheimer V., 2018, Phys. Rev. C, 98, 055805
Roark J., Du X., Constantinou C., Dexheimer V., Steiner A. W., Stone J. R., 2019, Monthly Notices of the Royal Astronomical Society, 486, 5441
Sekiguchi Y., Kiuchi K., Kyutoku K., Shibata M., 2011, Phys. Rev. Letts., 107, 211101
Sharma S., 2019, in Proceedings of The 36th Annual International Symposium on Lattice Field Theory — PoS(LATTICE2018). Sissa Medialab, doi:10.22323/1.334.0009
Shen H., Toki H., Oyamatsu K., Sumiyoshi K., 2011, The Astrophysical Journal Supplement Series, 197, 20
Steiner A. W., Lattimer J. M., Brown E. F., 2013, The Astrophysical Journal, 765, L5
Stergioulas N., Friedman J. L., 1995, Astrophysics Journal, 444, 306
Stone J. R., 2016, European Physical Journal A, 52, 66
Stone J. R., Stone N. J., Moszkowski S. A., 2014, Phys. Rev. C, 89, 044316
Stone J. R., Guichon P. A. M., Reinhard P. G., Thomas A. W., 2016, Physical Review Letters, 116, 092501
Stone J. R., Morita K., Guichon P. A. M., Thomas A. W., 2019, Physical Review C, 100
Sumiyoshi K., Ishizuka C., Ohnishi A., Yamada S., Suzuki H., 2009, Astrophysical Journal, 690, L43
Tan H., Noronha-Hostler J., Yunes N., 2020, arXiv:2006.16296

Tews I., Carlson J., Gandolfi S., Reddy S., 2018, The Astrophysical Journal, 860, 149
Tolman R. C., 1939, Phys. Rev., 55, 364
Torres-Forné A., Cerdá-Durán P., Obergaulinger M., MÃijller B., Font J. A., 2019, Physical Review Letters, 123
Tsang M. B., et al., 2012, Phys. Rev. C, 86, 015803
Typel S., 2020, New GRDF model with hyperons (working)
Typel S., Röpke G., Klähn T., Blaschke D., Wolter H. H., 2010, Physical Review C, 81, 015803
Wei J. B., Figura A., Burgio G. F., Chen H., Schulze H. J., 2019, J. Phys.G., 46, 034001
Weih L. R., Most E. R., Rezzolla L., 2019, The Astrophysical Journal, 881, 73
Weissenborn S., Chatterjee D., Schaffner-Bielich J., 2012, Physical Review C, 85
Yagi K., Yunes N., 2013, Science, 341, 365
Yoshida J., et al., 2019, in Proceedings of the 8th International Conference on Quarks and Nuclear Physics (QNP2018). Journal of the Physical Society of Japan, doi:10.7566/jpscp.26.023006